

Geometry-based approximation of waves propagating through complex domains*

Davide Pradovera[†]

Monica Nonino[†]

Ilaria Perugia[†]

February 1, 2023

Abstract

We consider wave propagation problems over 2-dimensional domains with piecewise-linear boundaries, possibly including scatterers. Under the assumption that the initial conditions and forcing terms are radially symmetric and compactly supported (which is common in applications), we propose an approximation of the propagating wave as the sum of some special nonlinear space-time functions: each term in this sum identifies a particular ray, modeling the result of a single reflection or diffraction effect. We describe an algorithm for identifying such rays automatically, based on the domain geometry. To showcase our proposed method, we present several numerical examples, such as waves scattering off wedges and waves propagating through a room in presence of obstacles.

Keywords: wave propagation, model reduction, scattering, geometrical optics, diffraction

AMS subject classifications: 35L05, 35Q60, 65M25, 78A45, 78M34

1 Introduction

The discretization of numerical models for the simulation of complex phenomena results in high-dimensional systems to be solved, usually at an extremely high cost in terms of computational time and storage memory. Among these models, wave propagation problems represent an extremely interesting topic: relevant applications can be found, e.g., in the field of array imaging, where acoustic, electromagnetic, and elastic waves in scattering media are modeled by the *reflectivity* coefficient, which is often unknown. Some examples in this direction can be found in [5, 6, 7, 30], where inverse scattering problems are used to infer the reflectivity of one or more scatterers embedded either in a known and smooth medium, or in a randomly inhomogeneous medium. Another example of application of wave propagation problems is numerical acoustics, where the goal is to simulate the propagation of sound in a room, in presence of obstacles and walls with different absorbing and/or reflecting properties, see [28].

Wave propagation problems in the time-harmonic setting (the *Helmholtz* problem, cast in the *frequency domain*) have been widely studied. See, e.g., [4, 13, 19, 24, 25, 27, 28]. However, our focus here are problems in the *time domain*, whose numerical simulation is expensive, mainly because one needs to use both a fine spatial mesh and a carefully chosen time step in order to satisfy the CFL condition [11, 16]. In the interest of making these simulations feasible, model order reduction (MOR) [3, 9, 14, 17] represents a promising framework, whose goal is to reduce the computational cost of solving the problem of interest.

In this context, it is well known [12, 15] that wave propagation problems are characterized by a slowly decaying Kolmogorov n -width. Because of this, classical linear-subspace MOR methods are not able to reproduce the behavior of the wave propagation without relying on a very high-dimensional linear manifold. This makes linear surrogate models unappealing, since they do not yield significant speed-ups. In recent years, many approaches have been proposed to overcome the intrinsic “difficulty” of problems with slowly

*M. Nonino and I. Perugia have been funded by the Austrian Science Fund (FWF) through project F 65 “Taming Complexity in Partial Differential Systems” and project P 33477.

[†]Faculty of Mathematics, University of Vienna, Oskar-Morgenstern-Platz 1, 1090 Vienna, Austria (davide.pradovera@univie.ac.at, monica.nonino@univie.ac.at, ilaria.perugia@univie.ac.at).

decaying Kolmogorov n -width, with the target of making MOR more efficient. To this end, such methods rely on nonlinear and/or hybrid space-time approaches. For more details, we refer to [8, 10, 18, 21, 26, 29, 31].

In this work, we focus on wave propagation over 2-dimensional spatial domains, possibly including obstacles. We limit our investigation to domains with piecewise-linear boundaries and a constant wave speed. The initial conditions and forcing terms are assumed to be compactly supported and radially symmetric around a “source point”. This situation arises in many of the above-mentioned applications. Under these assumptions, we propose to approximate the solution of the problem of interest with the sum of some special nonlinear space-time functions, which we call “rays”. Each ray models a reflection or diffraction effect, and is composed of different parts:

- the *free-space radially symmetric solution* of the wave equation, modeling the space-time propagation of the ray;
- a spatial indicator function, determining the *light cone* of each ray;
- a nonlinear spatial term encoding the *angular modulation* of the ray, which is crucial when modeling diffraction effects.

The number of terms appearing in the sum is determined by the number of reflection and diffraction effects that are required to faithfully approximate the target wave, which ultimately depends on the geometry of the physical domain.

Among the advantages of the proposed approach, we mention the fact that each ray is separable into time-radial and angular components (in the “polar coordinates” sense). As we will see, we can leverage this to reduce drastically the computational cost and the storage memory that are required by our approximation, with respect to competitor methods.

The rest of the paper is structured as follows. In Section 1.1 we present the problem of interest. In Section 2 we introduce the main ingredients of our method, and we describe the “training phase” of the algorithm, i.e., the construction of the approximated wave. In Sections 3 and 4 we detail how we model reflection and diffraction effects, respectively. The latter section is rather extensive, since diffraction is much harder to model than reflection, and requires special care. In Section 5 we present some numerical results to showcase our method. Both simple benchmarks (wedges) and more complicated tests (2D room model with scatterers) are considered. Some final considerations follow in Section 6.

1.1 Target problem

We are interested in the numerical approximation of the solution of the wave equation in complex domains. In this work, we consider 2-dimensional domains only. However, most of our discussion generalizes to 3D. We defer a discussion on this till Section 6.

We denote by $\Omega \subset \mathbb{R}^2$ the physical domain in which the wave equation is considered. We assume that Ω is either a closed polygon or a set-subtraction of polygons (to allow for multiply connected domains). We denote by n_e and n_v the number of edges and vertices of $\partial\Omega$, respectively. We study the propagation of waves in Ω over a given time interval of interest $[0, T]$. The model problem is the wave equation with constant (unit) wave speed:

$$\begin{cases} \partial_{tt}u(\mathbf{x}, t) = \Delta u(\mathbf{x}, t) + f(\mathbf{x}, t) & \text{for } (\mathbf{x}, t) \in \Omega \times (0, T), \\ u(\mathbf{x}, 0) = u_0(\mathbf{x}) & \text{for } \mathbf{x} \in \Omega, \\ \partial_t u(\mathbf{x}, 0) = u_1(\mathbf{x}) & \text{for } \mathbf{x} \in \Omega, \\ \partial_\nu u(\mathbf{x}, t) = 0 & \text{for } (\mathbf{x}, t) \in \partial\Omega \times (0, T], \end{cases} \quad (1)$$

with Δ the Laplacian operator, defined, in 2 dimensions, as $\Delta = \sum_{j=1}^2 \partial_{x_j x_j}$. The homogeneous Neumann condition (i.e., the last equation above) models the whole boundary $\partial\Omega$ as *sound-hard* [11]. More generally, all or parts of $\partial\Omega$ may be modeled as *sound-soft* via a Dirichlet-type condition: $u(\mathbf{x}, t) = 0$.

We assume that the initial conditions u_0 and u_1 , as well as the forcing term f , have radial symmetry around a given point. Without loss of generality, we will take such point to be the origin of \mathbb{R}^2 :

$$u_0(\mathbf{x}) = \eta_0(\|\mathbf{x}\|), \quad u_1(\mathbf{x}) = \eta_1(\|\mathbf{x}\|), \quad f(\mathbf{x}, t) = \eta_2(\|\mathbf{x}\|, t) \quad \forall (\mathbf{x}, t) \in \Omega \times (0, T), \quad (2)$$

with $\|\mathbf{x}\|^2 = \sum_{j=1}^2 x_j^2$. We further assume that the functions η_j have compact support, namely, that there exist $R > 0$ such that $\eta_j(\rho) = 0$ for all $\rho > R$ and $j = 0, 1, 2$. Moreover, to avoid incompatibilities with the boundary conditions, for simplicity we will only consider the situation where the supports of the functions η_j are fully contained in Ω .

2 Approximation framework

Before we can model boundary effects (reflection and diffraction), we need to understand how the solution u would behave if no boundary were present. To this aim, we consider the wave equation in free space

$$\begin{cases} \partial_{tt}U(\mathbf{x}, t) = \Delta U(\mathbf{x}, t) + f(\mathbf{x}, t) & \text{for } (\mathbf{x}, t) \in \mathbb{R}^2 \times (0, \infty), \\ U(\mathbf{x}, 0) = u_0(\mathbf{x}) & \text{for } \mathbf{x} \in \mathbb{R}^2, \\ \partial_t U(\mathbf{x}, 0) = u_1(\mathbf{x}) & \text{for } \mathbf{x} \in \mathbb{R}^2, \end{cases} \quad (3)$$

which we have obtained from (1) by replacing Ω with the whole plane.

Due to radial symmetry (of the initial conditions and of the forcing term), we can recast the problem in polar coordinates. This allows us to define the free-space solution in the radial coordinate Ψ , as the solution of

$$\begin{cases} \partial_{tt}\Psi(\rho, t) = \widehat{\Delta}\Psi(\rho, t) + \eta_2(\rho, t) & \text{for } (\rho, t) \in (0, \infty) \times (0, \infty), \\ \Psi(\rho, 0) = \eta_0(\rho) & \text{for } \rho \in [0, \infty), \\ \partial_t \Psi(\rho, 0) = \eta_1(\rho) & \text{for } \rho \in [0, \infty), \\ \partial_\rho \Psi(0, t) = 0 & \text{for } t \in (0, \infty), \end{cases} \quad (4)$$

where $\widehat{\Delta}$ is the Laplace operator in polar coordinates (under radial symmetry), i.e. $\widehat{\Delta} = \partial_{\rho\rho} + \frac{1}{\rho}\partial_\rho$, and $U(\mathbf{x}, t) = \Psi(\|\mathbf{x}\|, t)$ for all $\mathbf{x} \in \mathbb{R}^2$. Note that, by the compact support of the initial conditions and of the forcing term, and by the finite (unit) speed of propagation of the wave equation, we have $\Psi(\rho, t) = 0$ whenever $\rho > t + R$.

Remark 2.1. *Generally, the free-space solution Ψ is not available analytically, except for very simple choices of initial conditions and forcing term. Accordingly, in most applications, the function Ψ will need to be replaced with a suitable approximation. To this effect, one could discretize (4), e.g., with a finite element approximation (in space) and some timestepping scheme (in time). See Section 5 for more details on how this can be carried out.*

Our goal is to approximate, for all $(\mathbf{x}, t) \in \Omega \times [0, T]$, the solution $u(\mathbf{x}, t)$ of the wave equation problem (1) with the following sum of special functions:

$$u(\mathbf{x}, t) \approx \tilde{u}(\mathbf{x}, t) = \sum_{n=1}^N \underbrace{\Psi(\|\mathbf{x} - \xi_n\| + r_n, t) \mathbb{1}_{\Omega_n}(\mathbf{x}) \zeta_n(\mathbf{x} - \xi_n)}_{\tilde{u}_n(\mathbf{x}, t)}. \quad (5)$$

Each term \tilde{u}_n is what we will call a “ray”. Therein, Ψ is the above-mentioned free-space radially symmetric solution of (4), and $\mathbb{1}_A$ denotes the indicator function with support A , i.e.,

$$\mathbb{1}_A(y) = \begin{cases} 1 & \text{if } y \in A, \\ 0 & \text{if } y \notin A. \end{cases} \quad (6)$$

Moreover, in (5), we have introduced the following quantities:

- N is the number of rays used in the approximation.
- ξ_n is the location of the new source.
- $r_n \geq 0$ is a spatial delay, which will be used for the synchronization of diffraction effects.
- $\Omega_n \subset \Omega$ is the *light cone* (the spatial support) of a term of the sum.

- $\zeta_n : \mathbb{R}^2 \setminus \{\mathbf{0}\} \rightarrow \mathbb{R}$ is a weight function describing the angular modulation. We require that ζ_n be a positive-homogeneous functions, i.e., $\zeta_n(\mathbf{y}) = \zeta_n(\tau \mathbf{y})$ for all $\tau > 0$ and $\mathbf{y} \in \mathbb{R}^2$.

Note that, due to the finite speed of propagation of the free-space solution Ψ , we have that a generic term $\tilde{u}_n(\mathbf{x}, t)$ is zero whenever $t < \|\mathbf{x} - \xi_n\| + r_n - R$, i.e., for t small enough, depending on \mathbf{x} .

The number of rays N in the sum (5) will be determined based on how many boundary effects (reflections and diffractions) need to be included in \tilde{u} in order to have a good approximation of the target wave u . We describe a strategy for automatically identifying a good N in the next section. See, e.g., Remark 2.2.

2.1 Building the low-rank skeleton

Recalling that u solves the wave equation (1) in the domain Ω , we use the first term in (5), namely, \tilde{u}_1 , to approximate the outgoing component of u , *ignoring any effect due to the boundary $\partial\Omega$, except for shadows*. Then, given such \tilde{u}_1 , we use the other terms $\tilde{u}_2, \dots, \tilde{u}_N$ to correct this first approximation. Each extra term models a single effect due to a certain portion of the boundary, specifically, an edge (reflection off that edge) or a vertex (diffraction about that vertex).

Going back to the first ray \tilde{u}_1 , let us define it, by providing its “ingredients” ξ_1 , r_1 , Ω_1 , and ζ_1 , cf. (5). We set $\xi_1 = \mathbf{0}$, the center of the initial condition, as well as $r_1 = 0$, since no delay is necessary for this first term. Then, leveraging symmetry, we set $\zeta_1 \equiv 1$, which corresponds to the (physical) assumption that the propagation of \tilde{u}_1 is purely radial. Finally, we set Ω_1 (the light cone around $\mathbf{0}$) as the set of points that can be reached from $\mathbf{0}$ via a straight line without going outside $\partial\Omega$, i.e.,

$$\Omega_1 = \{\mathbf{x} \in \Omega : \tau \mathbf{x} \in \Omega \ \forall 0 \leq \tau \leq 1\}. \quad (7)$$

In summary, the first term of \tilde{u} is

$$\tilde{u}_1(\mathbf{x}, t) = \Psi(\|\mathbf{x}\|, t) \mathbb{1}_{\Omega_1}(\mathbf{x}). \quad (8)$$

Then we can move to the subsequent terms \tilde{u}_n , $n \geq 2$. Their expressions depend on our choice of reflection and diffraction modeling, and will be provided in the upcoming sections. Instead, in the rest of the present section we focus on understanding how large N should be, in order for \tilde{u} to provide a faithful approximation of u . Equivalently, we want to count the number of times the wave gets reflected or diffracted at the boundary $\partial\Omega$. This is done incrementally, starting from the initial value $N = 1$ (no boundary effects) and then updating this guess as more and more boundary effects get “discovered”.

To help us in this endeavor, we employ what we call a *timetable*, which, in this work, is simply a list of vectors, each with size $n_e + n_v$. The timetable is built incrementally starting from an empty list, appending one new vector every time a new term is added in the sum (5), starting from \tilde{u}_1 . The entries of the n -th timetable vector are the waiting times before \tilde{u}_n comes in contact with an edge or a vertex of $\partial\Omega$. If it is impossible for \tilde{u}_n to “cast light” (along a straight path) onto a certain edge or vertex, then the corresponding entry in the timetable is set to ∞ . After this, it suffices to look for the smallest not-yet-explored entry of the timetable to identify what the next term of the approximation \tilde{u} should be. Once the entry in the timetable has been explored, its value is set to ∞ .

We start by describing how the first vector $\mathbf{a}_1 \in \mathbb{R}^{n_e + n_v}$ of the timetable (corresponding to \tilde{u}_1) is computed, and how \mathbf{a}_1 allows us to identify the (geometric) features of \tilde{u}_2 . The vector \mathbf{a}_1 can be partitioned into edges-related part (the first n_e entries) and vertices-related part (the last n_v entries).

- **Edge times.** Given a generic edge $\gamma_j \subset \partial\Omega$ ($j = 1, \dots, n_e$) belonging to the domain boundary, we define the corresponding entry of \mathbf{a}_1 as

$$(\mathbf{a}_1)_j = \begin{cases} r_1 + \inf \{\|\mathbf{x} - \xi_1\| : \mathbf{x} \in \gamma_j \cap \bar{\Omega}_1\} & \text{if the set is non-empty,} \\ \infty & \text{otherwise.} \end{cases} \quad (9)$$

Note that we have taken the shortest path from ξ_1 to γ_j , and that we have denoted the closure of the light cone Ω_1 as $\bar{\Omega}_1$.

- **Vertex times.** Given a generic vertex $\mathbf{y}_j \subset \partial\Omega$ ($j = 1, \dots, n_v$) of the domain boundary, we set

$$(\mathbf{a}_1)_{n_e + j} = \begin{cases} r_1 + \|\mathbf{y}_j - \xi_1\| & \text{if } \mathbf{y}_j \in \bar{\Omega}_1, \\ \infty & \text{otherwise.} \end{cases} \quad (10)$$

Note that we have included the delay r_1 (which is actually zero here) as a way to streamline Eqs. (9) and (10) for the upcoming section. See Fig. 1 for a diagram showcasing these formulas.

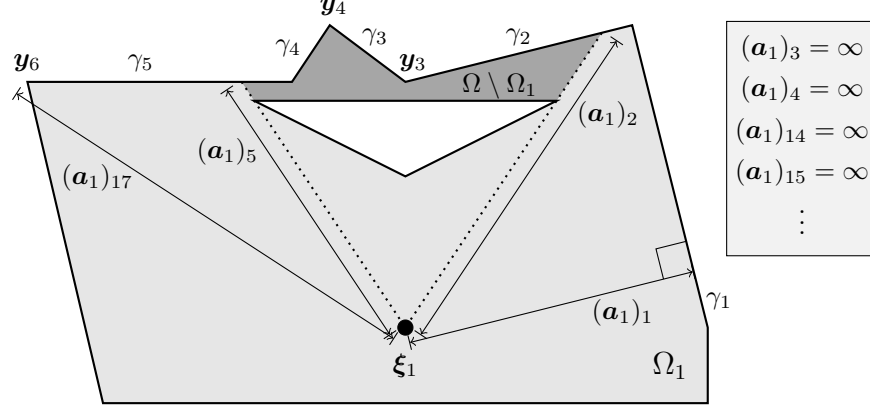


Figure 1: Computation of some timetable entries. The boundary $\partial\Omega$ has 11 sides, so that, e.g., $(\mathbf{a}_1)_14$ is related to \mathbf{y}_3 and $(\mathbf{a}_1)_17$ is related to \mathbf{y}_6 . The shadowed area $\Omega \setminus \Omega_1$ is in darker grey.

The smallest entry of \mathbf{a}_1 is the time at which the first “boundary event” (reflection or diffraction) can happen¹. The index of the smallest entry tells us whether the event is a reflection ($1 \leq j \leq n_e$) or a diffraction ($n_e + 1 \leq j \leq n_e + n_v$), and also what edge/vertex causes the event. From here, we use the models described in Sections 3 and 4 to build \tilde{u}_2 , by computing ξ_2 , r_2 , Ω_2 , and ζ_2 .

Then, the second timetable vector \mathbf{a}_2 can be computed by replacing all subscripts “1” by “2” in Eqs. (9) and (10). This is followed by the construction of \tilde{u}_3 , and so on. The process continues until all not-yet-explored entries of the timetable are larger than $T + R$. Indeed, starting from this time instant, the would-be next terms of \tilde{u} do not affect the approximation anymore, since, due to the finite speed of wave propagation, they only act (on Ω) after the end of the time horizon, i.e., for $t > T$. The total number of rays N is simply the number of vectors in the timetable.

We summarize the overall procedure for the construction of the rays \tilde{u}_n in Algorithm 1. For ease of presentation, once an entry of the timetable has been explored, it is set to ∞ as a way for the algorithm to ignore it from that point forward.

Algorithm 1 Step-by-step construction of the surrogate model

```

Set  $N \leftarrow 1$ , find  $\Omega_1$  as in (7), and define  $\tilde{u}_1$  as in (8)
Define  $\mathbf{a}_1 \in \mathbb{R}^{n_e+n_v}$  using Eqs. (9) and (10)
Set  $i \leftarrow 1$  and  $j \leftarrow \arg \min_{j=1,\dots,n_e+n_v} (\mathbf{a}_1)_j$ 
while  $(\mathbf{a}_i)_j \leq T + R$  do
  Set  $(\mathbf{a}_i)_j \leftarrow \infty$  and  $N \leftarrow N + 1$ 
  if  $j \leq n_e$  then
    Find  $\xi_N$ ,  $r_N$ ,  $\Omega_N$ , and  $\zeta_N$  as in Section 3
    ← Reflection from edge  $j$ 
  else
    Find vertex index  $j' \leftarrow j - n_e$ 
    Find  $\xi_N$ ,  $r_N$ ,  $\Omega_N$ , and  $\zeta_N$  as in Section 4
    ← Diffraction from vertex  $j'$ 
  end if
  Define  $\tilde{u}_N$  from  $\xi_N$ ,  $r_N$ ,  $\Omega_N$ , and  $\zeta_N$ , as in (5)
  Define  $\mathbf{a}_N \in \mathbb{R}^{n_e+n_v}$  using Eqs. (9) and (10), with “ $N$ ” replacing “1” in subscripts
  Set  $(i, j) \leftarrow \arg \min_{i=1,\dots,N, j=1,\dots,n_e+n_v} (\mathbf{a}_i)_j$ 
end while

```

¹We say “can happen” since not all vertices can cause diffraction, when hit from a certain point source. This issue is discussed in Section 4, cf. Assumption 4.3.

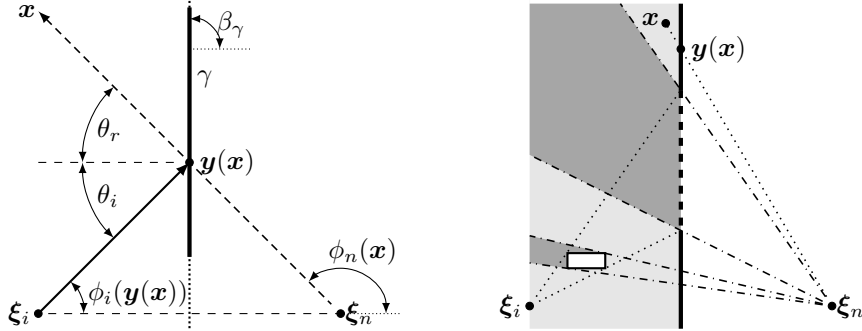


Figure 2: Graphical representation of a reflection off edge γ . On the left, the law of reflection prescribes $\theta_r = \theta_i$. We show the straight line $\tilde{\gamma}$ supporting γ with a dotted stroke. For a given observation point \mathbf{x} , $\mathbf{y}(\mathbf{x})$ denotes the point of incidence of the reflected ray. On the right, computation of the light cone Ω_n (light-grey area) and its complementary shadow zone $\Omega \setminus \Omega_n$ (dark-grey area) for the reflected ray, in the presence of a rectangular obstacle. The dashed portion of edge γ denotes the shadow $\gamma \setminus \gamma^{(i)}$. The shadow zone consists of two connected components.

Remark 2.2. In trapping domains, see, e.g., Section 5.2, the number of terms N might be rather large due to waves repeatedly “bouncing back and forth” between two or more edges/vertices. A large N , although necessary for a good approximation of all wavefronts, is undesirable since it increases the computational cost of both the construction of the surrogate \tilde{u} and its evaluation.

As a compromise, one could remove all terms \tilde{u}_n that are smaller than a certain tolerance tol , uniformly over \mathbf{x} and t . This can be done as a post-processing step (thus speeding up the evaluation of \tilde{u} but not its construction) or while building the surrogate itself. This can be achieved with a simple modification of Algorithm 1, by introducing a test on the magnitude of each soon-to-be-added wave contribution \tilde{u}_n , discarding terms that are too small.

3 Modeling reflection

We now present the strategy for modeling reflection due to an edge γ of the domain boundary $\partial\Omega$. We rely on the well-known *geometrical optics* model, which describes wave propagation in terms of rays, not accounting for any diffraction [23]. We assume that we are adding a new ray \tilde{u}_n to the surrogate model (5), due to a reflection phenomenon caused by ray \tilde{u}_i . Specifically, we assume that a ray coming from source point ξ_i hits the edge $\gamma \subset \partial\Omega$, i.e., that $\gamma \cap \overline{\Omega_i} \neq \emptyset$. We need to prescribe several ingredients.

Spatial correction r_n . We just transfer r_n over from the incoming wave: $r_n = r_i$. Indeed, as we will see in Section 4, we require the term r_n only when modeling diffraction.

Source point ξ_n . We use the method of images, which gives the position of ξ_n as the reflection of ξ_i with respect to the edge γ :

$$\xi_n = 2 \arg \min_{z \in \tilde{\gamma}} \|z - \xi_i\| - \xi_i, \quad (11)$$

where $\tilde{\gamma} \subset \mathbb{R}^2$ is the straight line on which edge γ lies. See Fig. 2 (left).

Weight function ζ_n . Let $\mathbf{x} - \xi_n$ be a generic point where we wish to evaluate the weight function ζ_n . We define the *incidence point* $\mathbf{y}(\mathbf{x})$ as the intersection (if any) between edge γ and the segment from ξ_n to \mathbf{x} . See Fig. 2 (left). According to the method of images, the amplitude of the reflected wave is equal (up to sign) to the amplitude of the incoming wave:

$$\zeta_n(\mathbf{x} - \xi_n) = (2\sigma_\gamma - 1)\zeta_i(\mathbf{y}(\mathbf{x}) - \xi_i). \quad (12)$$

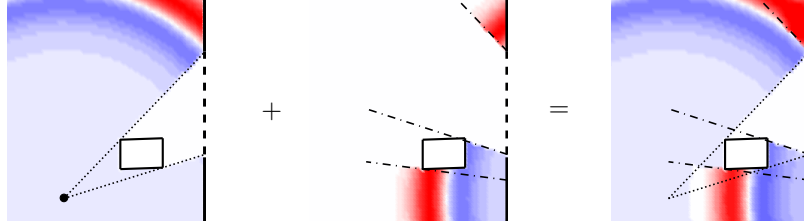


Figure 3: Example of reflection off an edge in the presence of an obstacle, from Fig. 2. Neumann conditions are imposed on all edges. Source wave (left), reflected wave (middle), and superimposition of the two (right). Note how the obstacle creates a shadow zone for source and reflected waves. For simplicity, in this plot we are not showing any reflection or diffraction effects due to the rectangular obstacle, since they would be modeled at different stages of the algorithm.

In the equation above, the quantity σ_γ is related to the kind of boundary conditions that are imposed on γ : if γ is an edge with Neumann boundary conditions, we set $\sigma_\gamma = 1$ (ζ_n and ζ_i have the same sign), whereas we set $\sigma_\gamma = 0$ if we have Dirichlet boundary conditions on γ (ζ_n and ζ_i have opposite signs).

Now, recall that we are assuming all weight functions to be positive-homogeneous: $\zeta_i(\mathbf{x} - \boldsymbol{\xi}_i) = \zeta_i(\tau(\mathbf{x} - \boldsymbol{\xi}_i))$, for all $\tau > 0$. Accordingly, as we are in 2D, $\zeta_i(\mathbf{x} - \boldsymbol{\xi}_i)$ is only a function of the direction (with sign) $v_i(\mathbf{x}) = (\mathbf{x} - \boldsymbol{\xi}_i)/\|\mathbf{x} - \boldsymbol{\xi}_i\|$, or, equivalently, of the angle $\phi_i(\mathbf{x})$ between $v_i(\mathbf{x})$ and the positive x_1 -axis. See Fig. 2 (left) for a graphical depiction. Specifically, with an abuse of notation, let $\zeta_i(\mathbf{x} - \boldsymbol{\xi}_i) = \zeta_i(\phi_i(\mathbf{x}))$ and $\zeta_n(\mathbf{x} - \boldsymbol{\xi}_n) = \zeta_n(\phi_n(\mathbf{x}))$, where the ‘‘new’’ angle-dependent functions ζ_i and ζ_n are 2π -periodic. By (12), we deduce the property

$$\zeta_n(\phi_n(\mathbf{x})) = (2\sigma_\gamma - 1)\zeta_i(\phi_i(\mathbf{y}(\mathbf{x}))) = (2\sigma_\gamma - 1)\zeta_i(2\beta_\gamma - \phi_n(\mathbf{y}(\mathbf{x}))) = (2\sigma_\gamma - 1)\zeta_i(2\beta_\gamma - \phi_n(\mathbf{x})), \quad (13)$$

where β_γ is the angle between edge γ and the positive x_1 -axis. This uniquely identifies ζ_n given ζ_i and β_γ .

Light cone Ω_n . We first identify what portion of γ is actually ‘‘lit’’ by \tilde{u}_i : $\gamma^{(i)} = \gamma \cap \overline{\Omega_i}$. Note that we may have $\gamma \neq \gamma^{(i)}$, for instance when obstacles are present between $\boldsymbol{\xi}_i$ and γ . See Fig. 2 (right) for an illustration. Then, roughly speaking, we define the new light cone Ω_n as the union of all rays from $\boldsymbol{\xi}_n$ that pass through $\gamma^{(i)}$. To be more precise, given $\mathbf{x} \in \Omega$, let $\mathbf{y}(\mathbf{x})$ be the intersection (if any) between γ and the line segment from $\boldsymbol{\xi}_n$ to \mathbf{x} . Also, if $\mathbf{y}(\mathbf{x})$ exists, we define $\tau_0(\mathbf{x}) = \|\mathbf{y}(\mathbf{x}) - \boldsymbol{\xi}_n\|/\|\mathbf{x} - \boldsymbol{\xi}_n\| \in (0, 1)$, which satisfies $\mathbf{y}(\mathbf{x}) = \boldsymbol{\xi}_n + \tau_0(\mathbf{x})(\mathbf{x} - \boldsymbol{\xi}_n)$. The new light cone is defined as

$$\Omega_n = \left\{ \mathbf{x} \in \Omega : \mathbf{y}(\mathbf{x}) \in \gamma^{(i)} \text{ and } \boldsymbol{\xi}_n + \tau(\mathbf{x} - \boldsymbol{\xi}_n) \in \Omega \quad \forall \tau_0(\mathbf{x}) < \tau \leq 1 \right\}. \quad (14)$$

Figure 3 represents a possible output of the numerical algorithm. In this case, we simulate only the reflections, thus discarding, for the time being, any effect due to diffraction. It is clear that, by modeling reflection effects only, we may obtain a discontinuous approximation of the solution of our target problem, where the discontinuity happens exactly at the *shadow boundaries* (the boundaries of light cones). As we will see in the next section, introducing diffraction in our approximation will allow us to obtain a continuous approximation \tilde{u} .

4 Modeling diffraction

Here, we describe a strategy for modeling waves diffracted by a vertex of the domain boundary $\partial\Omega$. This is required in building a new ray \tilde{u}_n whenever the smallest unexplored entry of the timetable is related to a vertex, i.e., $j > n_e$ in Algorithm 1, cf. Section 2. We need to identify several ingredients.

Source point $\boldsymbol{\xi}_n$. We employ the (standard, see, e.g., [23]) assumption that diffraction emerges as a wave outgoing from a point source located at the *diffraction point* $\mathbf{y}_{j-n_e} = \mathbf{y}_{j-n_e}$ (we are employing the notation of Algorithm 1). This motivates the choice of the center $\boldsymbol{\xi}_n = \mathbf{y}_{j-n_e}$.

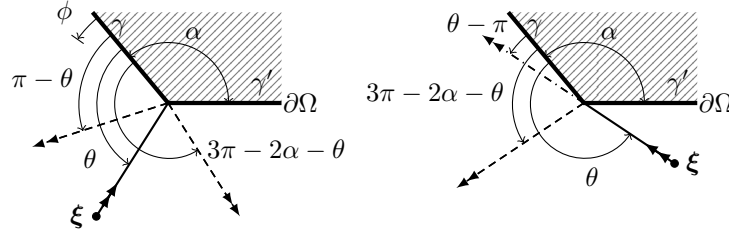


Figure 4: Diagrams for the two cases of scattering for concave corners ($0 < \alpha < \pi$): without (left plot) and with shadow zone (right plot). The dashed lines are reflection boundaries. The dash-dotted line is a shadow boundary. Shadow regions are absent if and only if $\pi - \alpha \leq \theta \leq \pi$. The angular coordinate $0 < \phi < 2\pi - \alpha$ is measured starting from one of the two adjacent edges of $\partial\Omega$.

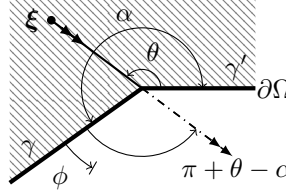


Figure 5: Diagrams for the scattering at convex corners ($\pi < \alpha < 2\pi$). The source point ξ is virtual, being used to model reflection off of edge γ . The dash-dotted line is the shadow boundary due to edge γ' . The shadow region is present if and only if $\alpha - \pi < \theta < \pi$. The angular coordinate $0 < \phi < 2\pi - \alpha$ is measured starting from one of the two adjacent edges of $\partial\Omega$.

Light cone Ω_n . Since the diffracted wave propagates in all geometrically allowed directions, we define the support Ω_n as the set of all points that are visible (along straight-line paths) from ξ_n , i.e.,

$$\Omega_n = \{\mathbf{x} \in \Omega : \xi_n + \tau(\mathbf{x} - \xi_n) \in \Omega \ \forall 0 < \tau \leq 1\}. \quad (15)$$

Modeling diffraction is substantially more complicated than modeling reflection. For this reason, before we can describe how the remaining unknown quantities r_n and ζ_n are defined, cf. (5), we need to introduce several assumptions.

Assumption 4.1 (Separability). *Diffracted waves are separable into radial-temporal and angular components around the diffraction point ξ_n . Otherwise stated, $\tilde{u}_n(\mathbf{x}, t)$ can be expressed (at least locally) as $\psi_n(\|\mathbf{x} - \xi_n\|, t)\zeta_n(\mathbf{x} - \xi_n)$, where ζ_n is positive-homogeneous, i.e., $\zeta_n(\mathbf{z})$ is independent of $\|\mathbf{z}\|$ (as long as $\mathbf{z} \neq \mathbf{0}$). Using an abuse of notation, we will express ζ_n as a function of ϕ only, with ϕ defined as the angular coordinate around ξ_n . See Figs. 4 and 5.*

This, together with the following assumption on the angular component ζ_n , will allow us to recover the approximation structure presented in Section 2.

Assumption 4.2 (Piecewise-linear angular component). *The angular component ζ_n is a piecewise-linear function of the angular coordinate ϕ , with discontinuities at all reflection and shadow boundaries. Using the geometrical optics approximation, we can explicitly compute the locations of such discontinuities:*

- at concave corners (see, e.g., Fig. 4), $\phi_1 = |\pi - \theta| = \max\{\pi - \theta, \theta - \pi\}$ and $\phi_2 = 2\pi - \alpha - |\pi - \alpha - \theta| = \min\{\theta + \pi, 3\pi - 2\alpha - \theta\}$;
- at convex corners (see, e.g., Fig. 5), $\phi_3 = \pi + \theta - \alpha$.

Now we are ready to describe our full diffraction model, which satisfies Assumptions 4.1 and 4.2, as well as the following three standard requirements.

Assumption 4.3 (Characterization of diffracting vertices). *A vertex ξ_n emits a diffraction wave in “response” to \tilde{u}_i only if both following conditions are met:*

- ξ_n is visible from ξ_i , i.e., $\xi_n \in \overline{\Omega}_i$;
- one of the following is true:
 - the domain Ω is locally concave near ξ_n , with ξ_i being located on the “concave side” of ξ_n , i.e., $0 < \alpha < \pi$ and $0 \leq \theta \leq 2\pi - \alpha$ in Fig. 4;
 - the domain Ω is locally convex near ξ_n and a “shadow zone” is present, i.e., $\pi < \alpha < 2\pi$ and $\pi - \alpha < \theta < \pi$ in Fig. 5.

or

- the domain Ω is locally convex near ξ_n and a “shadow zone” is present, i.e., $\pi < \alpha < 2\pi$ and $\pi - \alpha < \theta < \pi$ in Fig. 5.

Assumption 4.4 (Continuity of the full approximation). *The full wave approximation \tilde{u} is continuous, in particular across reflection and shadow boundaries.*

Assumption 4.5 (Conservation of mass). *Diffracted waves have zero “net mass”, i.e., $\int_{\mathbb{R}^2} \tilde{u}_n(\mathbf{x}, t) d\mathbf{x} = 0$, leading to mass conservation of the full wave approximation \tilde{u} . (Note that we are stating mass conservation in free space to ignore further reflections and diffractions of \tilde{u}_n , which are also assumed to conserve mass.)*

Spatial correction r_n . As in Algorithm 1, let i be the index of the term \tilde{u}_i that causes the diffraction \tilde{u}_n . With the objective of satisfying (5) and Assumption 4.4, we define the radial component ψ_n as

$$\psi_n(\|\mathbf{x} - \xi_n\|, t) = \Psi(\|\mathbf{x} - \xi_n\| + \underbrace{\|\xi_n - \xi_i\| + r_i}_{=: r_n}, t). \quad (16)$$

By direct inspection of this definition, we can see that, by our choice of r_n , we are “aligning” the wavefronts of the diffracted waves with the wavefronts of the reflected wave at the reflection boundaries (the shadow boundary of the reflected waves, if any) and with the wavefronts of the incoming wave \tilde{u}_i at its shadow boundary (if any). For instance, it is easy to see that, using (16), a point close to the diffraction point ($\mathbf{x} \approx \xi_n$) is within the support of the diffracted wave \tilde{u}_n only for $t \geq r_n - R$, i.e., only when the wave \tilde{u}_i has crossed the distance from ξ_i to ξ_n .

Weight function ζ_n . According to Assumption 4.2, we define the discontinuous piecewise-linear function $\zeta_n : [0, 2\pi - \alpha] \rightarrow \mathbb{R}$ as

$$\zeta_n(\phi) = \begin{cases} \frac{z_1(\phi_1 - \phi) + z_2\phi}{\phi_1} & \text{for } 0 < \phi < \phi_1 := |\pi - \theta|, \\ \frac{z_3(\phi_2 - \phi) + z_4(\phi - \phi_1)}{\phi_2 - \phi_1} & \text{for } \phi_1 < \phi < \phi_2 := 2\pi - \alpha - |\pi - \alpha - \theta|, \\ \frac{z_5(2\pi - \alpha - \phi) + z_6(\phi - \phi_2)}{2\pi - \alpha - \phi_2} & \text{for } \phi_2 < \phi < 2\pi - \alpha, \end{cases} \quad (17)$$

for concave corners, and

$$\zeta_n(\phi) = \begin{cases} \frac{z_1(\phi_3 - \phi) + z_7\phi}{\phi_3} & \text{for } 0 < \phi < \phi_3 := \pi + \theta - \alpha, \\ \frac{z_8(2\pi - \alpha - \phi) + z_6(\phi - \phi_3)}{2\pi - \alpha - \phi_3} & \text{for } \phi_3 < \phi < 2\pi - \alpha, \end{cases} \quad (18)$$

for convex corners. The scalars z_1, \dots, z_8 are nodal values of ζ_n : $\zeta_n(0) = z_1$, $\zeta_n(\phi_1^+) = z_3$ for concave corners, $\zeta_n(\phi_3^-) = z_7$ for convex corners, etc. These values are chosen so as to satisfy:

- The boundary conditions at the edges ending at ξ_n , i.e., γ and γ' .
- Assumption 4.4 at the discontinuity angles ϕ_1 , ϕ_2 , and ϕ_3 . To this aim, we prescribe values for the jumps $(z_3 - z_2)$, $(z_5 - z_4)$, and $(z_8 - z_7)$.
- Assumption 4.5. Given the radial-angular decomposition of \tilde{u}_n from Assumption 4.1, this is equivalent to the condition $\int_0^{2\pi - \alpha} \zeta_n(\phi) d\phi = 0$.

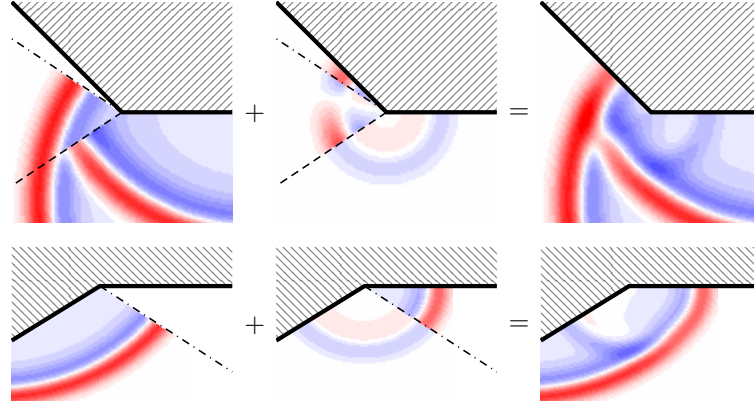


Figure 6: Examples of diffraction at the concave (top) and convex (bottom) corners from Fig. 4 (right) and Fig. 5. Neumann conditions are imposed on all edges. In each row of plots, we have: discontinuous wave without diffraction (left), diffraction wave (middle), and continuous wave with diffraction (right). Note that, in the convex case, we are not showing the wave \tilde{u}_i that causes the reflection off edge γ nor the reflection and scattering of \tilde{u}_i off edge γ' .

In the case of a convex corner, this set of condition uniquely identifies the four degrees of freedom. See Section 4.1 for the formulas and for their derivation. However, in the case concave case, an additional condition is required. In this work, we set this last condition as described in Section 4.2. We show in Fig. 6 the results obtained with our diffraction modeling in two simple illustrative cases.

Before proceeding further, we deem it important to make the following remark.

Remark 4.6. *Our proposed strategy is able to deliver only a fairly crude approximation of diffraction effects. (We refer to Section 5.1 for a validation of our model.) However, it has the great advantage of being extremely simple to build and to evaluate. Thanks to the modularity of our approach, it would be surely possible to replace our diffraction model with more sophisticated ones (e.g., removing Assumptions 4.1 and 4.2), in the interest of achieving a better approximation of the exact solution. To this aim, we mention that a wide body of works has been dedicated to the modeling of diffraction in the time-harmonic (Helmholtz) setting: among others, we name the geometrical [20] and uniform [23] theories of diffraction. However, the authors have not been able to find any satisfactory all-purpose time-domain diffraction modeling in the literature.*

4.1 Convex diffraction coefficients

Consider the situation depicted in Fig. 5 and the notation introduced therein. Also, we rely on the quantities ξ_n , r_n , Ω_n , and i introduced in Section 4. For diffraction to happen, cf. Assumption 4.3, \tilde{u}_i must be a wave reflected off either edge γ or γ' . Indeed, a convex vertex ξ_n cannot be “hit” from outside the domain Ω by the source wave \tilde{u}_1 , nor by any wave reflected off a different edge, nor by any diffracted wave centered at some vertex of $\partial\Omega$.

For this reason, the shadow boundary $\{\phi = \phi_3\}$ must belong to $\partial\Omega_i$ (the boundary of the light cone Ω_i), at least locally around ξ_n . Without loss of generality, we assume that \tilde{u}_i is a wave reflected off edge γ , so that Ω_i consists (locally) of point whose angular coordinate is $0 < \phi < \phi_3$. This means that $\phi_3 < \phi < 2\pi - \alpha$ is a shadow zone. The alternative case (of reflection off edge γ') can be obtained by symmetry.

Let $\sigma_\gamma = 0$ if γ is a Dirichlet edge and $\sigma_\gamma = 1$ if it is a Neumann edge. Define $\sigma_{\gamma'}$ similarly for edge γ' . To satisfy the conditions described in Section 4, the quantities z_1, z_7, z_8, z_6 appearing in the angular weight ζ_n , cf. (18), must satisfy the conditions:

- Boundary condition at γ : $z_1 = \sigma_\gamma z_7$.
- Boundary condition at γ' : $z_6 = \sigma_{\gamma'} z_8$.
- For \tilde{u} to be continuous at $\phi = \phi_3$, there must be a jump to account for the fact that \tilde{u}_i is nonzero for $\phi \rightarrow \phi_3^-$ but zero for $\phi \rightarrow \phi_3^+$: given the angular component of \tilde{u}_i at the shadow boundary, namely,

$h_i := \zeta_i(\xi_n - \xi_i)$, we impose $z_8 - z_7 = h_i$.

- Conservation of mass: for all $t > 0$,

$$\begin{aligned} 0 &= \int_{\mathbb{R}^2} \tilde{u}_n(\mathbf{x}, t) d\mathbf{x} = \int_0^\infty \int_0^{2\pi-\alpha} \psi_n(\rho, t) \zeta_n(\phi) \rho d\phi d\rho \\ &= \left(\int_0^{2\pi-\alpha} \zeta_n(\phi) d\phi \right) \left(\int_0^\infty \psi_n(\rho, t) \rho d\rho \right) \\ &= \left(\frac{z_1 + z_7}{2} \phi_3 + \frac{z_8 + z_6}{2} (2\pi - \alpha - \phi_3) \right) \left(\int_0^\infty \psi_n(\rho, t) \rho d\rho \right), \end{aligned}$$

which leads to the condition $\frac{z_1 + z_7}{2} \phi_3 + \frac{z_8 + z_6}{2} (2\pi - \alpha - \phi_3) = 0$.

With simple algebra, we now obtain

$$z_7 = \frac{(\sigma_{\gamma'} + 1)h_i(\phi_3 + \alpha - 2\pi)}{(\sigma_{\gamma'} + 1)(2\pi - \alpha) + (\sigma_\gamma - \sigma_{\gamma'})\phi_3}, \quad z_8 = \frac{(\sigma_\gamma + 1)h_i\phi_3}{(\sigma_{\gamma'} + 1)(2\pi - \alpha) + (\sigma_\gamma - \sigma_{\gamma'})\phi_3}, \quad (19)$$

as well as $z_1 = \sigma_\gamma z_7$ and $z_6 = \sigma_{\gamma'} z_8$. See Fig. 6 (bottom) for an example of the resulting diffraction wave.

4.2 Concave diffraction coefficients

Consider the setup depicted in Fig. 4 and the notation introduced therein. Also, we rely on the quantities ξ_n , r_n , Ω_n , and i introduced in Section 4. Let $\sigma_\gamma = 0$ if γ is a Dirichlet edge and $\sigma_\gamma = 1$ if it is a Neumann edge. Define $\sigma_{\gamma'}$ similarly for edge γ' . Without loss of generality, we assume that $0 < \theta \leq \pi - \frac{\alpha}{2}$, since the other case can be easily obtained by symmetry. In this setting, γ is in the light cone of \tilde{u}_i (at least locally around ξ_n). Accordingly, let $\tilde{u}_{i'}$ be the wave component obtained by reflection of \tilde{u}_i off edge γ .

If $0 < \theta \leq \pi - \alpha$, γ' is not in the light cone of \tilde{u}_i , so that:

- for $0 < \phi < \phi_1 = \pi - \theta$, both \tilde{u}_i and $\tilde{u}_{i'}$ are present;
- for $\phi_1 < \phi < \phi_2 = \pi + \theta$, only \tilde{u}_i is present, since the light cone $\Omega_{i'}$ ends at $\{\phi = \phi_1\}$;
- for $\phi_2 < \phi < 2\pi - \alpha$, neither \tilde{u}_i nor $\tilde{u}_{i'}$ is present, i.e., we have a shadow zone, since the light cone $\Omega_{i'}$ ends at $\{\phi = \phi_2\}$.

Otherwise, assume that $\pi - \alpha < \theta \leq \pi - \frac{\alpha}{2}$. In this case, γ' is also in the light cone of \tilde{u}_i (at least locally around ξ_n). We denote the wave component obtained by reflection of \tilde{u}_i off edge γ' by $\tilde{u}_{i''}$. Then:

- for $0 < \phi < \phi_1 = \pi - \theta$, both \tilde{u}_i and $\tilde{u}_{i'}$ are present;
- for $\phi_1 < \phi < \phi_2 = 3\pi - 2\alpha - \theta$, only \tilde{u}_i is present, since the light cones $\Omega_{i'}$ and $\Omega_{i''}$ end at $\{\phi = \phi_1\}$ and at $\{\phi = \phi_2\}$, respectively;
- for $\phi_2 < \phi < 2\pi - \alpha$, both \tilde{u}_i and $\tilde{u}_{i''}$ are present.

To satisfy the conditions described in Section 4, the quantities z_1, \dots, z_6 appearing in the angular weight ζ_n , cf. (17), must satisfy the conditions:

- Boundary condition at γ : $z_1 = \sigma_\gamma z_2$.
- Boundary condition at γ' : $z_6 = \sigma_{\gamma'} z_5$.
- For \tilde{u} to be continuous at $\phi = \phi_1$, there must be a jump whose height is the angular component of $\tilde{u}_{i'}$ at $\phi = \phi_1$, i.e., $h_{i'} := \zeta_{i'}(\xi_n - \xi_{i'})$; we impose $z_3 - z_2 = h_{i'}$. Note that, by the law of reflection, cf. (11), $h_{i'} = \tau h_i$, with $\tau = 2\sigma_\gamma - 1$ and $h_i := \zeta_i(\xi_n - \xi_i)$.
- For \tilde{u} to be continuous at $\phi = \phi_2$, there must be a jump whose height depends on whether $\theta \leq \pi - \alpha$ or not:

- If $0 < \theta \leq \pi - \alpha$, the jump equals the angular component of \tilde{u}_i at $\phi = \phi_2$, i.e., $h_i := \zeta_i(\xi_n - \xi_i)$; we impose $z_5 - z_4 = h_i$.
- If $\pi - \alpha < \theta \leq \pi - \frac{\alpha}{2}$, the jump equals minus the angular component of $\tilde{u}_{i''}$ at $\phi = \phi_2$, i.e., $h_{i''} := \zeta_{i''}(\xi_n - \xi_{i''})$; we impose $z_5 - z_4 = -h_{i''}$. Note that, by the law of reflection, cf. (11), $h_{i''} = (2\sigma_{\gamma'} - 1)h_i$, with $h_i := \zeta_i(\xi_n - \xi_i)$.

In summary, $z_5 - z_4 = \tau'h_i$, with $\tau' = 1$ if $0 < \theta \leq \pi - \alpha$ and $\tau' = 1 - 2\sigma_{\gamma'}$ if $\pi - \alpha < \theta \leq \pi - \frac{\alpha}{2}$.

- Conservation of mass: for all $t > 0$,

$$\begin{aligned} 0 &= \int_{\mathbb{R}^2} \tilde{u}_n(\mathbf{x}, t) d\mathbf{x} = \int_0^\infty \int_0^{2\pi-\alpha} \psi_n(\rho, t) \zeta_n(\phi) \rho d\phi d\rho \\ &= \left(\int_0^{2\pi-\alpha} \zeta_n(\phi) d\phi \right) \underbrace{\left(\int_0^\infty \psi_n(\rho, t) \rho d\rho \right)}_{=:C(t)} \\ &= \left(\frac{z_1 + z_2}{2} \phi_1 + \frac{z_3 + z_4}{2} (\phi_2 - \phi_1) + \frac{z_5 + z_6}{2} (2\pi - \alpha - \phi_2) \right) C(t), \end{aligned}$$

which leads to the condition $\frac{z_1 + z_2}{2} \phi_1 + \frac{z_3 + z_4}{2} (\phi_2 - \phi_1) + \frac{z_5 + z_6}{2} (2\pi - \alpha - \phi_2) = 0$.

One constraint is missing for the values z_1, \dots, z_6 to be uniquely determined. Specifically, some simple algebra shows that, for any $\delta \in \mathbb{R}$, the following set of values satisfies all the above conditions:

$$z_2 = \frac{\tau h_i + \delta}{(\sigma_{\gamma'} \phi_1 + \phi_2)/(\phi_1 - \phi_2)}, \quad z_5 = \frac{\tau' h_i + \delta}{(\phi_1 + \sigma_{\gamma'} \phi_2 - (\sigma_{\gamma'} + 1)(2\pi - \alpha))/(\phi_1 - \phi_2)}, \quad (20)$$

together with $z_1 = \sigma_{\gamma'} z_2$, $z_3 = z_2 + \tau h_i$, $z_4 = z_5 - \tau' h_i$, and $z_6 = \sigma_{\gamma'} z_5$. Note that the jump heights τh_i and $\tau' h_i$ appear in the numerators of z_2 and z_5 , respectively.

Our diffraction model is simply the one given by $\delta = 0$. Intuitively, this corresponds to a “balanced” partitioning of the mass of the diffracted wave into the components related to the two (reflection and/or shadow) boundaries ϕ_1 and ϕ_2 . See Fig. 6 (top) for an example of the resulting diffraction wave.

To further highlight the (mostly beneficial) effects of the choice $\delta = 0$, we note that:

- in the symmetric case $\theta = \pi - \frac{\alpha}{2}$, $\delta = 0$ leads to a symmetric ζ_n : $(1 - 2\sigma_{\gamma'})z_2 = (1 - 2\sigma_{\gamma'})z_5$;
- in the case $\theta = \pi - \alpha$, the second transition happens at γ' , i.e., $\phi_2 = 2\pi - \alpha$, and the choice $\delta = 0$ yields $z_4 = 0$, so that the diffraction wave vanishes at γ' (which is physically sound);
- in the “grazing incidence” case $\theta = 0$, the two transition coalesce into one, i.e., $\phi_1 = \phi_2$, and the choice $\delta = 0$ leads to $\zeta_n(\phi) = 0$ for all ϕ , which is unphysical; see the following remark for a possible solution.

Remark 4.7. In the “grazing incidence” case $\theta = 0$ (which corresponds to $\phi_1 = \phi_2 = \pi$), the diffraction wave \tilde{u}_n does not cure the discontinuity of \tilde{u} at the boundary $\{\phi = \pi\}$. This is because, in some sense, the two discontinuities of \tilde{u}_n at ϕ_1 and ϕ_2 cancel each other out. For a similar reason, a small $\theta \approx 0$ will result in a continuous total wave, but a sharp gradient will be present for $\phi_1 < \phi < \phi_2$.

By tweaking the value of δ , we can obtain an alternative diffraction model, which guarantees Assumption 4.4 even in the case of grazing incidence. To this aim, we can set

$$\begin{aligned} \delta &= \left((\sigma_{\gamma'} + 1) \frac{\sigma_{\gamma'} \phi_1 + \phi_2 - (\sigma_{\gamma'} + 1)(2\pi - \alpha)}{(\sigma_{\gamma'} - \sigma_{\gamma'})\phi_1 + (\sigma_{\gamma'} + 1)(2\pi - \alpha)} \phi_1 \tau + \right. \\ &\quad \left. + (\sigma_{\gamma'} + 1) \frac{\phi_1 + \sigma_{\gamma'} \phi_2}{(\sigma_{\gamma'} - \sigma_{\gamma'})\phi_2 + (\sigma_{\gamma'} + 1)(2\pi - \alpha)} (\phi_2 - 2\pi + \alpha) \tau' \right) \frac{h_i}{\phi_1 - \phi_2}. \quad (21) \end{aligned}$$

Roughly speaking, this corresponds to a different “balancing” of the mass of the diffracted wave into the components related to the two boundaries ϕ_1 and ϕ_2 .

This being said, in our numerical tests, such alternative model, albeit recovering a continuous total wave, resulted in a reduced accuracy of approximation. Specifically, using the value of δ above, we have observed an exaggerated magnitude of the diffraction wave, especially in the shadow zone.

Example index	exterior angle α	incidence angle ω	$\ \tilde{u}(\cdot, T)\ _{L^2(\Omega)}$	$\ \tilde{u}(\cdot, T) - u_{\text{FEM}}(\cdot, T)\ _{L^2(\Omega)}$
#1	4.712	0.984		$3.65 \cdot 10^{-4}$
#2	5.093	0.603		$2.02 \cdot 10^{-3}$
#3	2.761	1.363	$2.50 \cdot 10^{-1}$	$1.05 \cdot 10^{-2}$
#4	2.761	3.277		$2.00 \cdot 10^{-2}$

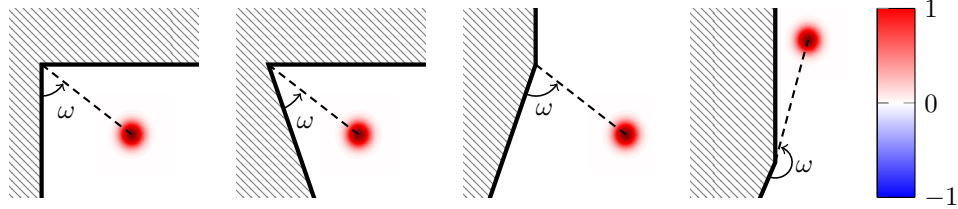
Table 1: Setup for the four wedge examples. The angle ω is as in Fig. 7.

Figure 7: Initial conditions for the wedge examples, indexed #1 through #4 from left to right. The (dashed) distance between the center of the Gaussian and the boundary vertex is 4 units in all cases.

5 Numerical results

In our experiments, we require a “reference” solution of (1) to validate our results. To this effect, we use the solution u_{FEM} obtained by discretizing (1) with:

- the P1-finite element method (P1-FEM) with mass-lumping, over a regular triangulation (mesh) of the physical domain Ω ;
- explicit leapfrog timestepping with a uniform time step that satisfies the CFL condition on the chosen mesh.

See [11, 16] for more details on this discretization strategy.

If the domain Ω is unbounded, we first need to truncate it in such a way that reflections from the non-physical truncation boundary do not affect the solution in the region of interest for $t < T$. Recalling that the problem data are supported in a ball of radius R and center $\mathbf{0}$, this can be done, e.g., by truncating Ω at the sphere with radius $R + T$ and center $\mathbf{0}$. In our tests, we rely on FEniCS [1] to carry out the P1-FEM discretization on 2-dimensional domains Ω .

Instead, note that with our proposed approach, modeling unbounded domains is straightforward. Indeed, we can simply ignore any reflection or diffraction from its “infinitely far” vertices/edges.

All our tests are performed in Python 3.8 on a machine with an 8-core 3.60 GHz Intel® processor and 64 GB of RAM. For reproducibility, our code is made available at <https://github.com/pradovera/ray-wave-2d>.

5.1 Some simple wedges

As a way to assess our proposed method in simple settings, we consider four different “wedge” domains. Similarly to the diagrams in Figs. 4 and 5, we define Ω to be one of the portions of the plane \mathbb{R}^2 delimited by straight lines intersecting at a point. Locally around such point, Ω “looks” like either Fig. 4 or Fig. 5, with α being the outer angle. The specific choices of wedge angles α are reported in Table 1 for the four cases.

We set up a problem of the form (1), with u_0 an isotropic Gaussian with standard deviation 0.2. The center of u_0 is at a point located at a 4-unit distance from the wedge vertex, in the direction determined by the “incidence angle” ω . See Fig. 7 for a representation of the initial conditions in the four cases. We set $u_1 = f = 0$, we enforce Neumann boundary conditions on the whole $\partial\Omega$, and we seek the solution at the final time $T = 5$, i.e., 1 time unit after the wave crest has reached the wedge vertex.

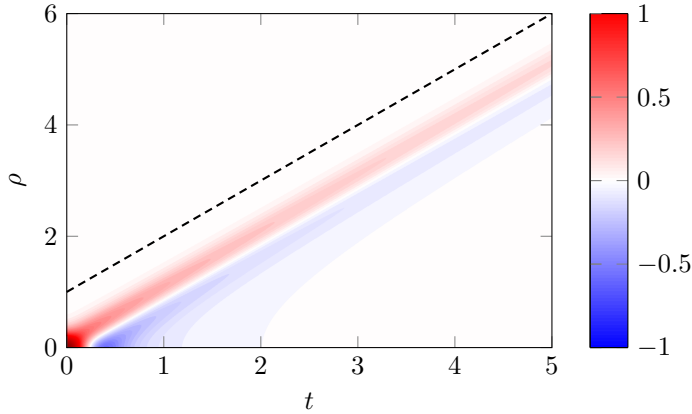


Figure 8: Free-space solution Ψ . The dashed line denotes the upper bound of the “causality cone” of Ψ , i.e., $\rho = t + R$, with $R = 1$.

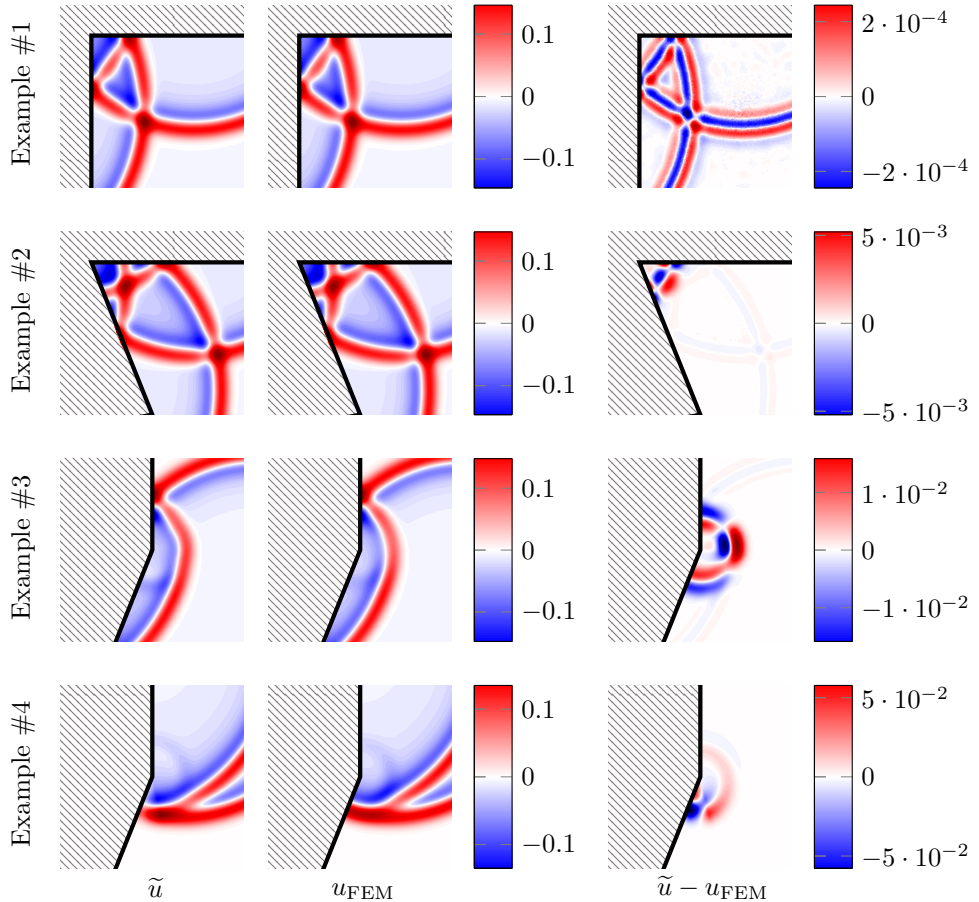


Figure 9: Results for the four wedge examples. Each row pertains to a different example. In each row, from left to right: surrogate solution \tilde{u} , FE solution, and error. The color scales for the first two columns are the same. All results are shown at the final time $t = T$.

To this aim, we employ our proposed approach, see Section 2. First, we compute an approximation of the free-space solution Ψ , which solves (4), by employing P1-FEM with explicit leapfrog timestepping. Note that, since (4) is cast in polar coordinates, we only need to discretize a 1D interval with P1-FEM. Since the initial condition u_0 is supported within the unit disk, we have $R = 1$, and it suffices to approximate $\Psi(\rho, t)$ for $(\rho, t) \in [0, T + R] \times [0, T]$. Since this space-time domain is only 2-dimensional, we can afford even a very fine discretization. In our experiments, we employ a 1001×2001 uniform Cartesian space-time grid, i.e., the mesh size is $\delta x = \frac{T+R}{1000}$ and the time step is $\delta t = \frac{T}{2000}$. This satisfies the CFL condition. We show the resulting Ψ (which, in fact, we should denote by Ψ_{FEM}) in Fig. 8.

After this preliminary step, we use the timetable-based strategy from Section 2 to identify reflection and scattering effects, which are then added up to give the final approximation \tilde{u} . We show the resulting $\tilde{u}(\cdot, T)$ in Fig. 9. In this figure, we also display a reference solution $u_{\text{FEM}}(\cdot, T)$, which we obtain by direct discretization of (1) by P1-FEM and leapfrog timestepping, as described at the beginning of Section 5.

In all four examples, we see that \tilde{u} and the reference u_{FEM} seem qualitatively close. Notably, we can observe a good representation of the most prominent wavefronts, which are due to propagation of either the main ‘‘free-space’’ wave or to its reflections. Indeed, those wave contributions are reconstructed exactly: the only errors are the ones due to FE approximation and timestepping, which affect both u_{FEM} and \tilde{u} (the latter through the approximation of Ψ). Instead, some differences are present when comparing diffraction effects, which arise as circular waves about the wedge vertex. We can quantitatively observe this in the last column of both Table 1 and Fig. 9.

In example #1, we observe a very small error, which, in fact, is simply the (FEM and timestepping) discretization error. This is related to the fact that the wedge has exterior angle $\alpha = \frac{3}{2}\pi$, which makes diffraction unnecessary in approximating the wave u : reflections are enough².

In the other examples, diffraction effects are necessary to correctly identify u . While a good qualitative behavior can be observed in Fig. 9, we can see in Table 1 that a modest error is present. Specifically, we report the $L^2(\Omega)$ -norm of \tilde{u} and of the error $\tilde{u} - u_{\text{FEM}}$ at the final time $t = T$, defined as

$$\|v\|_{L^2(\Omega)} = \left(\int_{\Omega} v(\mathbf{x})^2 d\mathbf{x} \right)^{1/2}. \quad (22)$$

We see the largest error in example #4, where the relative $L^2(\Omega)$ -approximation error amounts to 8%. This was to be expected, since this last example is rather close to the setting of grazing incidence ($\alpha + \omega \approx 2\pi$), which, as discussed in Section 4.2, is approximated rather poorly by our diffraction model. Qualitatively, the bad approximation quality is apparent in the form of a rather sharp gradient in the corresponding plot of \tilde{u} in Fig. 9 (bottom left).

5.1.1 Building a cavity out of wedges

As a slightly more complicated example, we now combine the four wedges from the previous section to obtain the open cavity represented in Fig. 10. In this case, more reflection and diffraction effects will arise, due to the trapping nature of the domain. Our initial conditions and forcing term are the same as before, but now all edges are sound-soft. Accordingly, we model them using Dirichlet boundary conditions. The time horizon is $T = 9$.

Using our strategy from Section 2, we build the approximation \tilde{u} , which contains 47 wave terms (1 source wave, 32 reflected waves, and 14 diffraction waves). We compare the approximation \tilde{u} with the reference solution u_{FEM} , obtained as described at the beginning of Section 5.

We show the results of the comparison in Fig. 10, at 4 time instants $t \in \{0, 3, 6, 9\}$. Once more, we see a good qualitative agreement between \tilde{u} and u_{FEM} , with the most important features of u being identified well. Up to $t = 3$, only reflections have happened, so that the error $\tilde{u} - u_{\text{FEM}}$ consists only of FEM and timestepping errors. On the other hand, for larger times, we see ‘‘error waves’’ of small-to-moderate amplitude propagating from the 3 vertices of Ω that generate diffraction effects. These correspond to errors in diffraction modeling.

²To intuitively understand why, let γ_1 and γ_2 be the two sides forming $\partial\Omega$. The domain Ω is partitioned *exactly* into (i) the light cone of the reflection off γ_1 and then off γ_2 and (ii) the light cone of the reflection off γ_2 and then off γ_1 . For this reason, the diffraction effects due to these two rays cancel out. Incidentally, the same phenomenon can be expected whenever the interior angle $2\pi - \alpha$ is of the form $\frac{\pi}{n}$, with $n \in \{2, 3, \dots\}$.

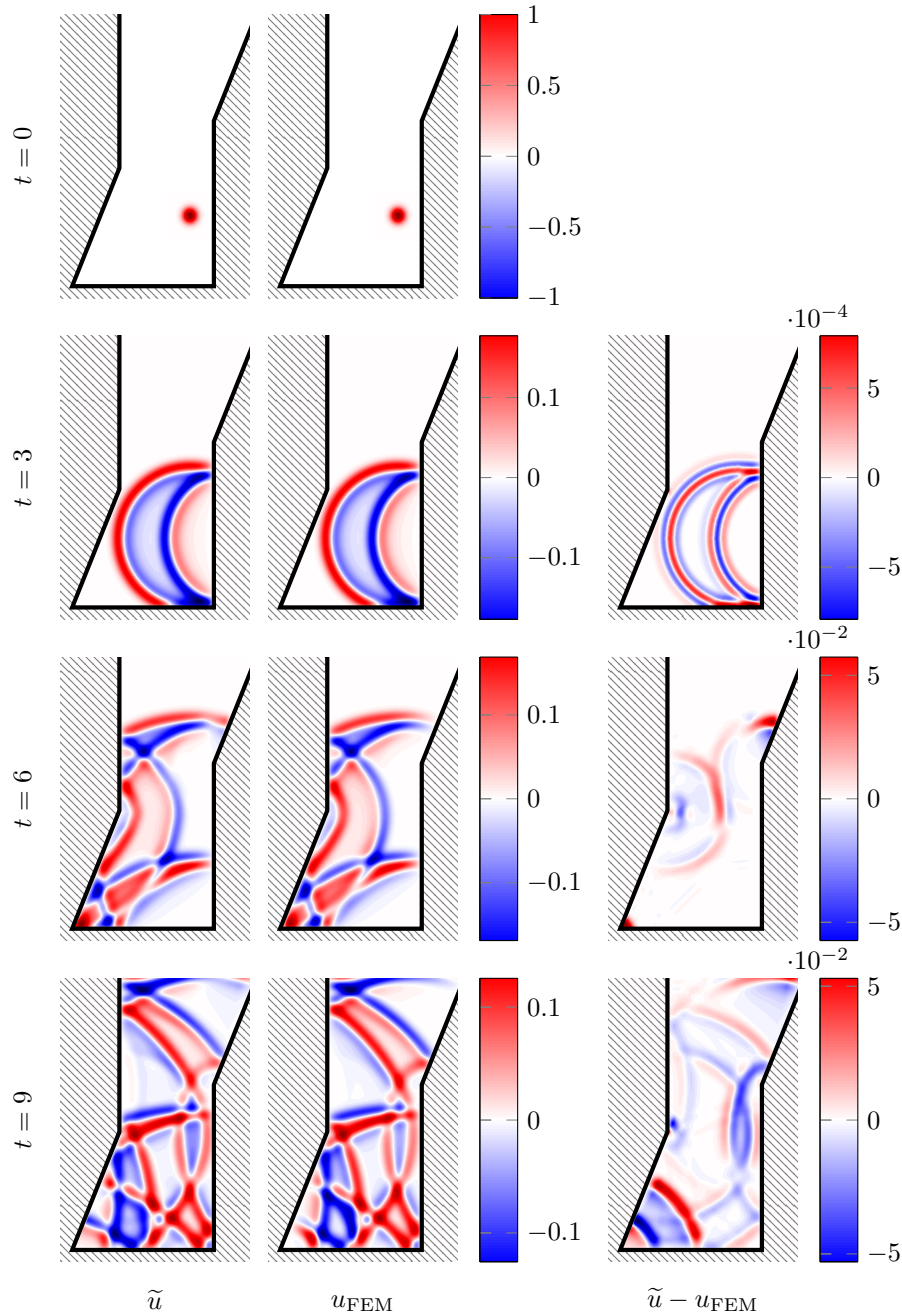


Figure 10: Results for the cavity domain. Each row corresponds to a different time instant $t \in \{0, 3, 6, 9\}$, from top to bottom. In each row, from left to right: surrogate solution $\tilde{u}(\cdot, t)$, FE solution $u_{\text{FEM}}(\cdot, t)$, and error $\tilde{u}(\cdot, t) - u_{\text{FEM}}(\cdot, t)$. The color scales for the first two columns are the same.

5.2 A tall room

We consider a simplified sound propagation problem in a room. For simplicity, we consider a 2-dimensional problem, thus assuming an infinitely tall room, and modeling line sources (in the z -direction) as point sources.

The complicated domain $\Omega \subset \mathbb{R}^2$ is depicted in Fig. 11. It is composed of two communicating “rooms” with sound-hard walls, as well as of a third large room (above), which is modeled as infinitely large. In the main room, three sound-soft triangular obstacles are also present.

Setting once more $u_1 = f = 0$, we are interested in modeling the propagation of an initial condition u_0 modeled as a Ricker wavelet centered at $\mathbf{0}$, see Fig. 11 (top left), over the time horizon $t \in [0, T]$, with $T = 20$. To this aim, we employ our proposed method from Section 2.

As in the previous example, we start by computing an approximation of the free-space solution $\Psi = \Psi(\rho, t)$ for $(\rho, t) \in [0, T + R] \times [0, T]$, see (4), with R being the radius of the support of the initial condition u_0 . Again, we use P1-FEM with leapfrog timestepping for this.

Since many reflective surfaces face each other, the domain Ω is trapping. Accordingly, we expect the number N of waves in the approximation \tilde{u} to be rather large. In the interest of reducing the number of such terms, we can employ the on-the-fly parsimonious strategy described in Remark 2.2, removing all wave terms \tilde{u}_n whose magnitude is smaller than $\text{tol} = 10^{-2}$. After this, $N \approx 1.4 \cdot 10^3$ terms are left. Although this value of N may seem large, the evaluation of the corresponding surrogate \tilde{u} is rather quick, due to the explicit nature of each wave contribution (and to the fact that their supports are smaller than the whole Ω).

We show the resulting $u(\cdot, t)$ for the four times $t \in \{0, 7.5, 15, 20\}$ in Fig. 11. There, we can see why so many terms are necessary for the approximation of u : we must model many reflection and diffraction effects. Since energy escapes the system only through the top “door”, the wave will persist for quite a long time. Accordingly, a larger T will make a larger N necessary.

In order to better inspect this effect, we show the trace of the solution at the arbitrarily chosen point $\mathbf{x}_{\text{trace}} = (-1, -2)$ in Fig. 12. We notice that oscillations persist for $t > 10$. We use this last plot also to validate our results. To this aim, we compare three results:

- The surrogate \tilde{u} obtained as described above, with $\text{tol} = 10^{-2}$.
- The surrogate \tilde{u} obtained with our strategy, but with $\text{tol} = 10^{-3}$. This leads to an increased number of rays $N \approx 7.3 \cdot 10^3$.
- The reference solution u_{FEM} obtained by the P1-FEM with leapfrog timestepping, as described at the beginning of Section 5. The mesh size must be chosen small enough to resolve both the initial condition and the domain Ω well. In our case, we have a mesh with approximately $1.4 \cdot 10^6$ elements. To satisfy the CFL condition on this mesh, we choose a time step $\Delta t \approx 7 \cdot 10^{-3}$.

We can observe that the two surrogates obtained with our approach give very similar results. Indeed, the cutoff tolerance tol affects the results only for large $t > 15$, due to the accumulation of “small” waves that are excluded from the coarser surrogate but included in the finer one.

Moreover, taking the FE solution as reference, we see that most of the peaks of the surrogates are aligned with the FE ones (i.e., the “phase” of the wave is well approximated), but there are some noticeable discrepancies in their amplitudes. This is due to the fact that, in our approach, reflection is modeled exactly, whereas the magnitudes of the diffraction waves are only roughly approximated. For this reason, we should not expect the amplitude error to get smaller if we reduce tol . The only “real” way of improving the approximation is using a better diffraction modeling.

As a final result, we also report:

- The so-called “offline” time, i.e., the time required to compute the numerical solution. For \tilde{u} , this means executing Algorithm 1. For u_{FEM} , this means building the mesh, assembling the FE stiffness and (lumped) mass matrices, and carrying out the timestepping.
- The so-called “online” time, i.e., the time required to evaluate the numerical solution (\tilde{u} or u_{FEM}) at a single (\mathbf{x}, t) -point.

They can be found in Table 2.

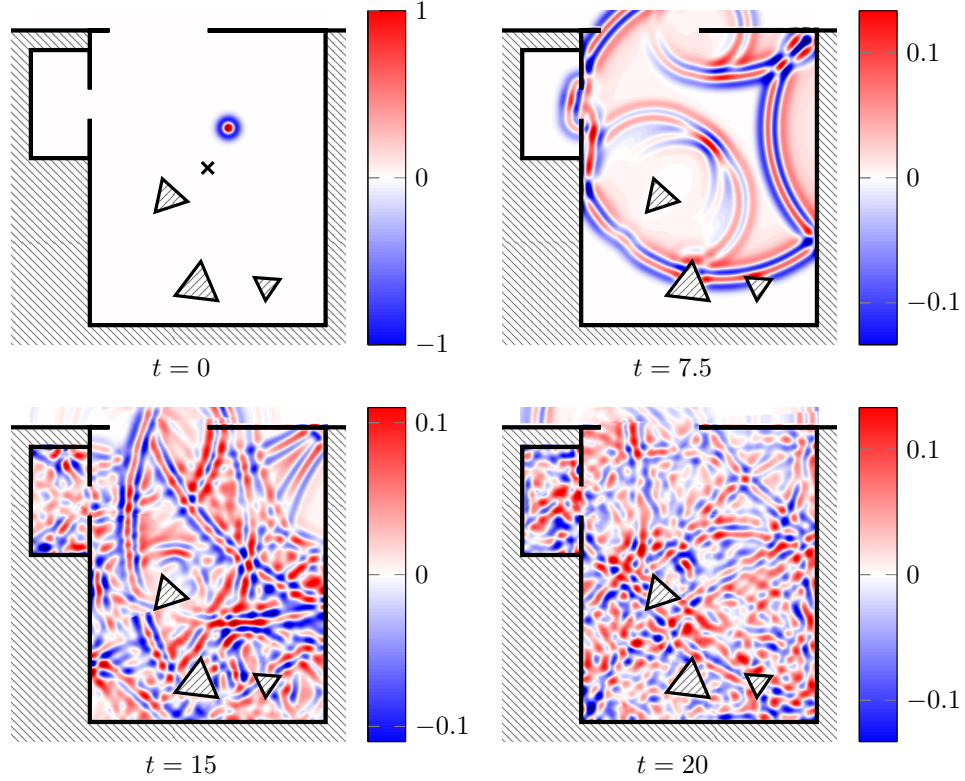


Figure 11: 2-dimensional domain Ω modeling a room. Top left plot: initial condition $\tilde{u}(\cdot, 0) = u(\cdot, 0) = u_0$, a Ricker wavelet; we also show the point x_{trace} as a cross. Top right plot: intermediate solution $\tilde{u}(\cdot, 7.5)$. Bottom left plot: intermediate solution $\tilde{u}(\cdot, 15)$. Bottom right plot: final solution $\tilde{u}(\cdot, 20)$.

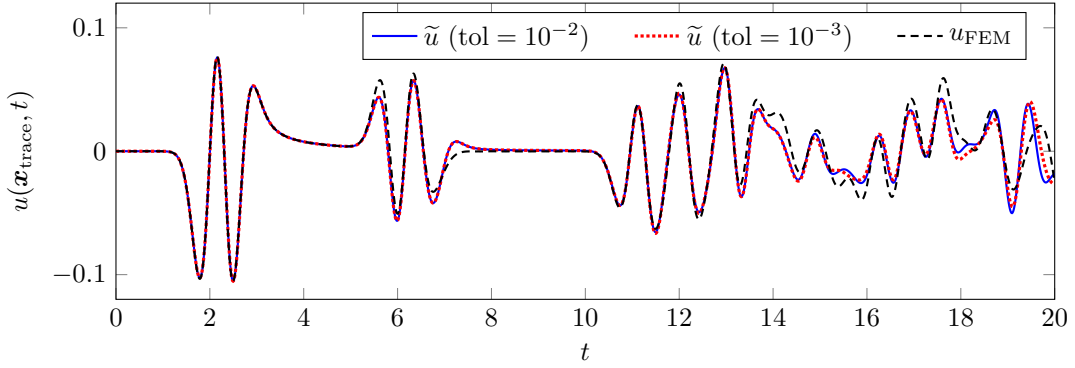


Figure 12: Value of solution at point $x_{\text{trace}} = (-1, -2)$.

Method	\tilde{u} (tol = 10^{-2})	\tilde{u} (tol = 10^{-3})	u_{FEM}
Offline	46.66 [s]	252.9 [s]	188.9 [s]
Online	2.04 [ms]	8.48 [ms]	27.67 [μ s]

Table 2: Timings for the room test case. To obtain more statistically significant results, each displayed time is the average over 3 (resp. 10^3) runs of the offline (resp. online) phase with identical parameters.

We can observe the increased training and evaluation time that results from decreasing tol . Moreover, we see that, in this example, our proposed approach is more competitive offline, but less so online. Somewhat surprisingly, we have observed that the most expensive step in evaluating \tilde{u} (taking about half of the online time) is determining whether an evaluation point is in the light cones Ω_n . The reason for this is that they can have rather complicated shapes, cf. Section 3.

Evaluating the FE solution at a space-time point is an extremely cheap operation (essentially corresponding to a vector dot product) while evaluating \tilde{u} is more expensive, requiring the evaluation of $\mathcal{O}(N)$ nonlinear functions. However, the FE solution comes with the serious drawback of memory usage. Indeed, in our example, storing u_{FEM} as a $(\sim 1.5 \cdot 10^6) \times (\sim 2.9 \cdot 10^3)$ array of double-precision floating-point numbers requires approximately 34 GB.

Concerning the timing results, we also wish to mention that the online times in Table 2 should be interpreted carefully. Indeed, the online time for the FE solution is artificially deflated by the fact that $\mathbf{x}_{\text{trace}}$ is a vertex of the FE mesh: each evaluation of u_{FEM} corresponds to extracting a vector entry. If $\mathbf{x}_{\text{trace}}$ had not been a vertex of the mesh, the online time could have been larger by at least one order of magnitude, if not more, depending on the FE implementation. Moreover, we note that accessing point-evaluations of u_{FEM} at arbitrary times *a posteriori*, namely, after the timestepping has been carried out, is feasible only if enough memory is available to store the whole “timestepping history”. Considering the numbers mentioned in the previous paragraph, this might not be possible in practice, especially for more complex and/or larger domains.

5.2.1 A time-harmonic source

One of the advantages of our approach is that it allows changing the source terms of the problem in a seamless way. Notably, under minor technical constraints (e.g., the support of the new source term should not be larger than the old one), this kind of change does not require training a new surrogate.

To showcase this, we approximate the wave propagating from a time-harmonic point source at $\mathbf{x} = \mathbf{0}$ with angular frequency $\omega > 0$. In our tests, we pick $\omega \in \{2\pi, 10\pi\}$. To this aim, we define u as the solution of the following (ω -dependent) problem:

$$\begin{cases} \partial_{tt}u(\mathbf{x}, t) = \Delta u(\mathbf{x}, t) - \omega^2 \sin(\omega t) \delta_{\mathbf{0}}(\mathbf{x}) & \text{for } (\mathbf{x}, t) \in \Omega \times (0, T), \\ u(\mathbf{x}, 0) = 0 & \text{for } \mathbf{x} \in \Omega, \\ \partial_t u(\mathbf{x}, 0) = 0 & \text{for } \mathbf{x} \in \Omega, \\ \partial_{\nu} u(\mathbf{x}, t) = 0 & \text{for } (\mathbf{x}, t) \in \partial\Omega \times (0, T], \end{cases} \quad (23)$$

where $\delta_{\mathbf{0}}$ denotes the usual 2-dimensional “delta function” centered at $\mathbf{x} = \mathbf{0}$.

As usual, we define $\Psi = \Psi(\rho, t)$ as the (ω -dependent) solution of the free-space version of (23) in radial-temporal coordinates. Note that, in free space, i.e., without boundary effects³, the forcing term in (23) is equivalent to the following non-homogeneous Dirichlet-like condition at $\rho = 0$:

$$U(\mathbf{0}, t) = \Psi(0, t) = \int_0^t \int_0^{t'} -\omega^2 \sin(\omega t'') dt'' dt' = \sin(\omega t) \quad \forall t > 0. \quad (24)$$

Accordingly, the free-space solution Ψ has space-time support $\{(\rho, t) \in [0, \infty)^2, \rho \leq t\}$, which is a subset of the free-space solution Ψ from the previous section, namely, $\{(\rho, t) \in [0, \infty)^2, \rho \leq t + R\}$. As such, to obtain an approximation for the wave u generated by the time-harmonic source for an arbitrary ω , it suffices to plug the corresponding Ψ in each term of the surrogate \tilde{u} from the previous section! We show the results of our approximation in Figs. 13 and 14.

We note that, if we had chosen to apply the FEM to approximate the wave u generated by the time-harmonic source, we would have been forced to carry out a new simulation from scratch for every frequency to be studied. To this end, we would have needed to choose a mesh with ω -dependent resolution: the mesh size should be small enough for the well-known *pollution effect* (see, e.g., [22, 2]) to be absent.

³If Ω is bounded, reflected or diffracted waves will generally bounce back to $\mathbf{x} = \mathbf{0}$. As such, the value of $u(\mathbf{0}, t)$, u being the solution of (23), will be different from the source signal $\sin(\omega t)$. For this reason, we cannot turn the forcing term in (23) into a condition like (24), except in free space.

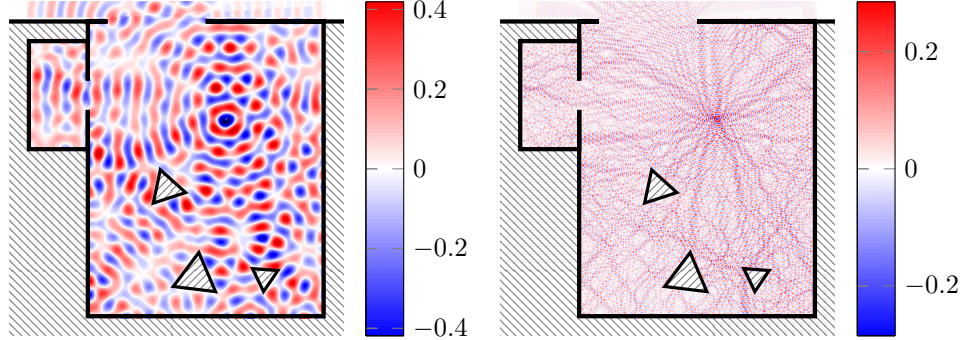


Figure 13: Surrogate solution found with the proposed approach. Left plot: $\omega = 2\pi$. Right plot: $\omega = 10\pi$.

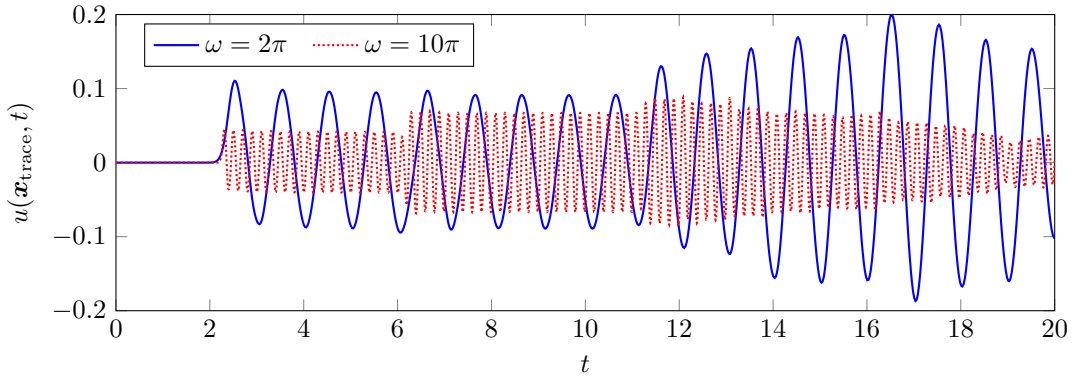


Figure 14: Value of solution at point $\mathbf{x}_{\text{trace}} = (-1, -2)$ for different excitation frequencies.

In our proposed approach, we also have a constraint on the mesh resolution. However, it only applies to the problem defining the free-space solution Ψ , which is 1-dimensional in space. Hence, having to refine the mesh represents a much smaller obstacle to efficiency. In particular, for a fixed time horizon T , the computation of \tilde{u} becomes more and more efficient, when compared to the computation of u_{FEM} , as the frequency ω increases.

6 Conclusions

We have presented a method for approximating waves propagating through complex 2-dimensional domains with polygonal boundaries. Our method relies on the automatic identification of reflection and diffraction effects caused by the domain geometry. Each effect is modeled through a relatively simple nonlinear expression. In our numerical tests, we have observed rather a good approximation quality, with the main features of the target wave being well identified. As a way to improve the approximation accuracy, we recall that any diffraction model could replace the current one.

In terms of complexity, our method requires the solution of a simplified 1D-in-space problem, much simpler than the original 2D-in-space one. We expect such improved accuracy to increase even further if one were to consider 3D instead of 2D problems. However, in order to generalize our method to 3 space dimensions, a suitable diffraction model would be necessary. This is one of our ongoing research directions.

Another favorable aspect of our algorithm is its potential to be run on parallel architectures, since the computation of different rays can be carried out independently. This is not the case for standard timestepping-based discretizations, due to their intrinsically sequential nature.

Other envisioned extensions of our technique involve the cases of domains with curvilinear boundaries and of propagation media with non-uniform properties (e.g., density and refraction index). Specifically, this latter case would effectively result in a non-uniform wave speed, with reflections and diffractions happening

also within the domain Ω .

Finally, we recall that, in many applications, the ultimate target is understanding how the wave u solving (1) depends on underlying parameters $\boldsymbol{\mu}$, e.g., the forcing term f , the shape of the domain Ω , etc. In this setting, MOR methods try to construct a surrogate model of the form $\tilde{u} = \tilde{u}(\mathbf{x}, t; \boldsymbol{\mu})$, providing a good approximation of u over a whole range of parameter values. Even though our technique was presented here in the non-parametric setting, we believe that it potentially allows incorporating the parameter dependence in a natural and efficient way. In our opinion, this might be achievable by leveraging the simple and interpretable structure of the rays (free-space solution, light cone, and angular modulation). As a simple preliminary example, we showcased this in Section 5.2.1 for a parametric source term, with the parameter being the frequency. We are currently investigating how to extend our method to more complicated parametric problems.

References

- [1] M. S. Alnæs, J. Blechta, J. Hake, and Others. The FEniCS Project version 1.5. *Archive of Numerical Software*, 3(100), 2015.
- [2] I. M. Babuška and S. A. Sauter. Is the pollution effect of the fem avoidable for the helmholtz equation considering high wave numbers? *SIAM Journal on Numerical Analysis*, 34(6):2392–2423, 1997.
- [3] P. Benner, M. Ohlberger, A. Cohen, and K. Willcox. *Model reduction and approximation: theory and algorithms*. SIAM, 2017.
- [4] F. Bonizzoni, F. Nobile, I. Perugia, and D. Pradovera. Least-Squares Padé approximation of parametric and stochastic Helmholtz maps. *Advances in Computational Mathematics*, 46(3):46, 2020.
- [5] L. Borcea, V. Druskin, A. V. Mamonov, and M. Zaslavsky. Robust nonlinear processing of active array data in inverse scattering via truncated reduced order models. *Journal of Computational Physics*, 381:1–26, 2019.
- [6] L. Borcea, V. Druskin, A. V. Mamonov, M. Zaslavsky, and J. Zimmerling. Reduced order model approach to inverse scattering. *SIAM Journal on Imaging Sciences*, 13(2):685–723, 2020.
- [7] L. Borcea, G. Papanicolaou, C. Tsogka, and J. Berryman. Imaging and time reversal in random media. *Inverse Problems*, 18(5), 2002.
- [8] P. Buchfink, S. Glas, and B. Haasdonk. Symplectic Model Reduction of Hamiltonian Systems on Nonlinear Manifolds. *arXiv preprint arXiv:2112.10815*, 2021.
- [9] P. Buchfink, B. Haasdonk, and S. Rave. PSD-Greedy Basis Generation for Structure-Preserving Model Order Reduction of Hamiltonian Systems. In *Proceedings of ALGORITMY*, pages 151–160, 2020.
- [10] N. Cagniart, Y. Maday, and B. Stamm. *Model Order Reduction for Problems with Large Convection Effects*, pages 131–150. Springer International Publishing, Cham, 2019.
- [11] G. Cohen, A. Hauck, M. Kaltenbacher, and T. Otsuru. Different Types of Finite Elements. In S. Marburg and B. Nolte, editors, *Computational Acoustics of Noise Propagation in Fluids - Finite and Boundary Element Methods*, pages 57–88. Springer Berlin Heidelberg, Berlin, Heidelberg, 2008.
- [12] R. A. DeVore. The theoretical foundation of reduced basis methods. *Model reduction and approximation: theory and algorithms*, 15:137, 2017.
- [13] S. Esterhazy and J. M. Melenk. On stability of discretizations of the Helmholtz equation. In *Numerical analysis of multiscale problems*, pages 285–324. Springer, 2012.
- [14] S. Glas, A. T. Patera, and K. Urban. A reduced basis method for the wave equation. *International Journal of Computational Fluid Dynamics*, 34(2):139–146, 2020.

- [15] C. Greif and K. Urban. Decay of the Kolmogorov N-width for wave problems. *Applied Mathematics Letters*, 96:216–222, 2019.
- [16] E. Hairer, G. Wanner, and C. Lubich. *Geometric Numerical Integration*, volume 31 of *Springer Series in Computational Mathematics*. Springer Berlin Heidelberg, Berlin, Heidelberg, 2002.
- [17] J. S. Hesthaven and C. Pagliantini. Structure-preserving reduced basis methods for Poisson systems. *Mathematics of Computation*, 90(330):1701–1740, 2021.
- [18] J. S. Hesthaven, C. Pagliantini, and N. Ripamonti. Rank-adaptive structure-preserving reduced basis methods for Hamiltonian systems. *arXiv preprint arXiv:2007.13153*, 2020.
- [19] R. Hiptmair, A. Moiola, and I. Perugia. Trefftz discontinuous Galerkin methods for acoustic scattering on locally refined meshes. *Applied numerical mathematics*, 79:79–91, 2014.
- [20] J. B. Keller. Geometrical theory of diffraction. *J. Opt. Soc. Am.*, 52(2):116–130, 1962.
- [21] K. Lee and K. T. Carlberg. Deep conservation: A latent-dynamics model for exact satisfaction of physical conservation laws. *Proceedings of the AAAI Conference on Artificial Intelligence*, 35(1):277–285, 2021.
- [22] S. Marburg. A Unified Approach to Finite and Boundary Element Discretization in Linear Time-Harmonic Acoustics. In S. Marburg and B. Nolte, editors, *Computational Acoustics of Noise Propagation in Fluids - Finite and Boundary Element Methods*, pages 1–34. Springer Berlin Heidelberg, Berlin, Heidelberg, 2008.
- [23] D. A. McNamara, C. W. I. Pistorius, and J. A. G. Malherbe. *Introduction to the uniform geometrical theory of diffraction*. Artech House Norwood, MA, 1990.
- [24] J. M. Melenk and S. Sauter. Wavenumber explicit convergence analysis for Galerkin discretizations of the Helmholtz equation. *SIAM Journal on Numerical Analysis*, 49(3):1210–1243, 2011.
- [25] A. Moiola, R. Hiptmair, and I. Perugia. Plane wave approximation of homogeneous Helmholtz solutions. *Zeitschrift für angewandte Mathematik und Physik*, 62(5):809–837, 2011.
- [26] C. Pagliantini. Dynamical reduced basis methods for Hamiltonian systems. *Numerische Mathematik*, 148(2):409–448, 2021.
- [27] S. F. Potter and M. K. Cameron. Jet marching methods for solving the eikonal equation. *SIAM Journal on Scientific Computing*, 43(6):A4121–A4146, 2021.
- [28] S. F. Potter, M. K. Cameron, and R. Duraiswami. Numerical geometric acoustics: an eikonal-based approach for modeling sound propagation in 3D environments. *arXiv preprint arXiv:2208.13002*, 2022.
- [29] J. Reiss, P. Schulze, J. Sesterhenn, and V. Mehrmann. The shifted proper orthogonal decomposition: A mode decomposition for multiple transport phenomena. *SIAM Journal on Scientific Computing*, 40(3):A1322–A1344, 2018.
- [30] P. H. Tournier, I. Aliferis, M. Bonazzoli, M. de Buhan, M. Darbas, V. Dolean, F. Hecht, P. Jolivet, I. El Kanfoud, C. Migliaccio, F. Nataf, C. Pichot, and S. Semenov. Microwave tomographic imaging of cerebrovascular accidents by using high-performance computing. *Parallel Computing*, 85:88–97, 2019.
- [31] G. Welper. Interpolation of functions with parameter dependent jumps by transformed snapshots. *SIAM Journal on Scientific Computing*, 39(4):A1225–A1250, 2017.